Journal of Hazardous Materials 373 (2019) 367–376

Contents lists available at ScienceDirect

Journal of Hazardous Materials

journal homepage: www.elsevier.com/locate/jhazmat

Metal – organic frameworks-derived MnO_2/Mn_3O_4 microcuboids with hierarchically ordered nanosheets and Ti_3C_2 MXene/Au NPs composites for electrochemical pesticide detection

Dandan Song, Xinyu Jiang, Yanshan Li, Xiong Lu, Sunrui Luan, Yuanzhe Wang, Yan Li, Faming Gao*

Key Laboratory of Applied Chemistry, Department of Applied Chemistry, Yanshan University, Qinhuangdao 066004, PR China

GRAPHICAL ABSTRACT

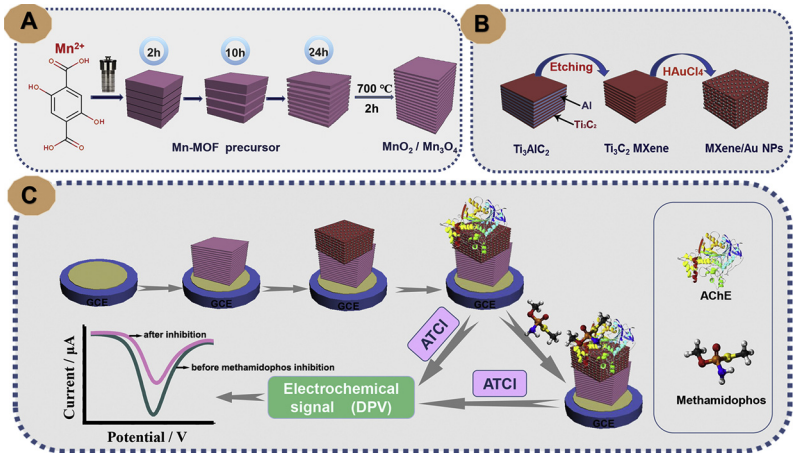

ARTICLE INFO

Keywords:
MOF-derived MnO_2/Mn_3O_4
Ti_3C_2MXene/Au NPs
AChE biosensor
Methamidophos

ABSTRACT

Transition metal oxides (TMOs) derived from metal – organic frameworks (MOF) combined with two-dimensional (2D) transition metal carbides possibly pave an innovative pathway for designing promising biosensors. Herein, a novel electrochemical sensing platform has been fabricated for ultra-sensitive determination of organophosphorus pesticides (OPs), based on MOF-derived MnO_2/Mn_3O_4 and Ti_3C_2 MXene/Au NPs composites. Remarkably, the three-dimensional (3D) MnO_2/Mn_3O_4 hierarchical microcuboids derived from Mn-MOF are composed of vertically aligned, highly ordered nanosheets, and further combined with MXene/Au NPs yields synergistic signal amplification effect, with outstanding electrochemical performance, large specific surface area, and good environmental biocompatibility. Under the optimum conditions, the reported sensing platform AChE-Chit/MXene/Au NPs/MnO_2/Mn_3O_4/GCE can be utilized to detect methamidophos in a broad concentration range (10^{-12}–10^{-6} M), together with a good linearity (R = 0.995). Besides that, the biosensor possesses a low limit of detection (1.34×10^{-13} M), which far exceeds the maximum residue limits (MRLs) for methamidophos (0.01 mg/kg) established by European Union. Additionally, the feasibility of the proposed biosensor for detecting methamidophos in real samples has been demonstrated with excellent recoveries (95.2%–101.3%). Interestingly, the unique structures and remarkable properties of these composites make them attractive

* Corresponding author.
E-mail address: gaofaming@ysu.edu.cn (F. Gao).

https://doi.org/10.1016/j.jhazmat.2019.03.083
Received 19 November 2018; Received in revised form 9 March 2019; Accepted 18 March 2019
Available online 23 March 2019

materials for various electrochemical sensors for monitoring either pesticide residuals or other environmentally deleterious chemicals.

1. Introduction

A wide array of environmental contaminants are routinely released into the environment resulting from agricultural activities. Organophosphate pesticides (OPs), are extensively used worldwide to increase agricultural productivity, whereas the excessive use of pesticides may trigger contamination in ecosystems and pose a great potential human health threat [1–3]. The high toxicity of pesticides is associated with their ability to irreversibly bind to acetylcholinesterase (AChE), which inhibit the activity of AChE and then could seriously destroy the human nervous system, eventually leading to organ failure and death [4–7]. Hence, it is of significant importance to devise an ultra-sensitive and accurate assay for the rapid screening of pesticide residues. The currently accepted standard techniques include the fluorescent bioprobes, high pressure liquid chromatography, antibody-based immunoassays, and chromatography coupled with mass spectrometry [8–13]. Despite these analytical technologies are sensitive and effective in the analysis of OPs, there exist several shortcomings of requirements of sophisticated instruments and skilled technicians, complex and time consuming sample pretreatment process, thus leading to high determination cost [14–17]. As a promising alternative, AChE-based biosensors have been developed for rapidly monitoring OPs compounds via enzymatic inhibition pathway, ascribed to their instrumental simplicity, moderate cost, high sensitivity, and selectivity [18–21].

Metal − organic frameworks (MOFs), structured by coordinating polytopic organic ligands with metal ions or clusters [22,23], have aroused tremendous interest for applications in energy storage, gas adsorption and desorption, chemical sensor and catalysis, owing to their promising features, including exceptionally large surface areas, highly ordered pores, adjustable internal surface properties and various functionalities [24,25]. In particular, the extraordinarily tunable structures and properties of MOF are expected to outperform other traditional chemo-sensory materials for constructing sensors [26,27]. Furthermore, various crystal structures of MOFs can be formed in accordance with the different coordination modes between the organic ligands and metal centers. MOFs can crystallize into particles, bulk as well as layered structures [28]. Notably, the layered MOF structure might show superiority than other crystal structures, as a result of its larger surface area as well as more accessible active sites on their surfaces. Unfortunately, most MOFs are natively along with poor electrical conductivity [29,30], which dramatically limits the efficient utilization of MOF in the fabrication of biosensors. Therefore, either translating to MOF derivative or combining MOFs with highly conductive materials is expected to further achieve improved electrochemical performance. More intriguingly, MOFs can be used as precursors to derive tailorable functional materials such as metal oxide and their carbon composites through thermal/chemical treatments [31–33]. Transition metal oxides (TMO) derived from MOFs possess good electrical conductivity and keep the same structure as the parent MOFs, as well as large surface areas [34], which make these electrochemically active materials desirable as electrode materials to achieve superior performance for constructing sensing platform.

Very recently, two-dimensional (2D) transition metal carbides (labelled MXenes), are a novel class of 2D materials produced by the extraction of the intermediate element from MAX phases, where M generally represents an early transition metal (e.g., Ti, Mo, Sc, Zr, Hf, V, Nb, Ta, Cr), A is an A group element (Al or Si), and X is either carbon or nitrogen [35,36]. Given their outstanding properties e.g., hydrophilicity, combined high electronic conductivity, high volumetric capacitance, superior electrochemical properties and extremely large specific surface areas, the MXenes have attracted great interest for a wide variety of applications in supercapacitors [37], electrocatalysis [38], fuel cells [39], lithium ion batteries [40], sensors [41,42] and hydrogen storage [43]. Moreover, embedded with noble metal (Au, Ag) nanoparticles could significantly tune MXene with improved conductivity and enhanced electrochemical properties, further exploiting their application to electrochemical biosensors.

Inspired by these considerations, in this contribution, highly conductive MOF-derived MnO_2/Mn_3O_4 and Ti_3C_2 MXene/Au NPs composites were prepared and employed as a sensing platform for electrochemical pesticide detection. As known, although ultrathin 2D nanomaterials have been extensively employed as electrode materials for constructing electrochemical sensors, there also exist disadvantages. It should be noted that these ultrathin nanomaterials possess low long-time stability and the nanosheets easily stacked attributed to their ultrathin nature [44]. Simultaneously, the nanomaterials lost some exposed active sites due to the stacking. To realize layered structure merits and long-time stability, multiple layers of composites are highly desirable. Herein, the MOF-derived MnO_2/Mn_3O_4 composites with a layered structure of stacked nanosheets were prepared for the first time. The MnO_2/Mn_3O_4 composed of vertically aligned, highly ordered nanosheets, not only provides an excessively large specific surface area for the electrochemical reactions, but also exhibits excellent electrochemical property and long-time stability. Especially to deserve to be mentioned, the combination of MnO_2/Mn_3O_4 and MXene/Au NPs is anticipated to realize synergistic signal amplification as a result of excellent performance of the AChE biosensor.

2. Experimental section

2.1. Materials and apparatus

Acetylcholinesterase (AChE; E.C.3.1.1.7; 518 U/mg protein) from Electrophorus electricus (electric eel) and acetylthiocholine chloride (ATCl) were purchased by Sigma-Aldrich (USA). Titanium aluminum carbide (Ti_3AlC_2, ≥ 98%) powder was purchased by Forsman Technology Company (Beijing, China). 2,5-dihydroxyterephthalic acid and $MnCl_2{\cdot}4H_2O$ were purchased from Aladdin. Methamidophos was obtained from LGC Promochem (Wesel, Germany). Chitosan (Chit), 1% (w/v), was prepared in 0.1 M acetic acid. Stock solutions of phosphate buffer saline (PBS, 0.1 M) were prepared by mixing 0.1 M Na_2HPO_4 and NaH_2PO_4 olutions. All chemicals and materials used in this work were of analytical reagent grade.

2.2. Characterizations

X-ray diffraction (XRD) patterns were performed with a Rigaku D/MAX-2500 powder X-ray diffractometer by Cu Ka (λ = 0.15406 nm, 40 kV, 200 mA). The morphology and structure of the composites were characterized by employing a scanning electron microscope (SEM, Hitachi S4800, Japan) and a transmission electron microscope (TEM, JEOL JEM-200EX, Japan). X-ray photoelectron spectrum was carried out to analyze the element and oxidation state of the composites by using a photoelectron spectrometer (Thermo Scientific ESCALAB 250Xi) employing Mg-Ka as X-ray source (1253.6 eV). Thermogravimetric analysis (TGA) was collected on a SDT Q600 thermoanalyzer under air atmosphere with a heating rate of 10 °C min^{-1}. Raman spectrum was recorded using a WITec, alpha300R.

2.3. Preparation of MOF-derived MnO_2/Mn_3O_4 composites

The MOF-derived MnO_2/Mn_3O_4 with layered structure was prepared for the first time. $MnCl_2{\cdot}4H_2O$ and 2,5-dihydroxyterephthalic acid were used as the precursors. Typically, $MnCl_2{\cdot}4H_2O$ (17.8 mg) together with 2,5-dihydroxyterephthalic acid (59.4 mg) was dissolved in a mixture of DMF-ethanol-water (30 ml, 15:1:1 (v/v/v)) and then poured into a 75 mL Teflon-lined stainless steel autoclave. Subsequently, it was heated at 135 °C for 24 h to synthesize Mn-MOF. After several hours of cooling down, the collected samples were centrifuged and washed with ethanol and water several times and dried in vacuum at 50 °C for 12 h. Finally, the collected precipitate was heat-treated at 700 °C in N_2 gas for 2 h to obtain the layered MOF-derived MnO_2/Mn_3O_4 composite.

2.4. Preparation of Ti_3C_2 MXene/Au NPs

The Ti_3C_2 MXene was synthesized via a conventional method (in Supplementary material) [45]. Ti_3C_2 MXene/Au NPs were prepared by following steps. 20 mg of Ti_3C_2 MXene was ultrasonically dissolved in 50 mL ultrapure water. Into this uniform suspension, 600 microliters of 100 mM $HAuCl_4$ aqueous solution was slowly added with mild shaking. After 10 min of reaction, the MXene/Au NPs suspension was then centrifuged at 5000 r.p.m. for 20 min and the collected precipitate was re-dispersed in absolute ethyl alcohol for further tests.

2.5. Fabrication of the AChE-Chit/MXene/Au NPs/MnO_2/Mn_3O_4/GCE

Prior to modify the electrode, the GCE was polished thoroughly with 0.3 μm and 50 nm alumina slurry, followed by ultrasonically washing with ethanol and water. 3 microliters of the suspension of MOF-derived MnO_2/Mn_3O_4 with appropriate concentration was dropped on freshly electrode surface and dried naturally. Then, 5 microliters of the suspension of MXene/Au NPs was further cast onto the MnO_2/Mn_3O_4 modified electrode. Finally, a mixture of AChE and Chit (1:6 (v/v) were next spread to the surface of MXene/Au NPs/MnO_2/Mn_3O_4/GCE. The modified electrode was stored in a refrigerator kept at 4 °C for further measurements.

2.6. Electrochemical measurements

Cyclic voltammetry (CV), differential pulse voltammetry (DPV), amperometric and electrochemical impedance spectroscopy (EIS) measurements were conducted on a CHI 750E electrochemical working station (Chenhua Apparatus Co., Shanghai, China) by a three-electrode system. A saturated calomel electrode (SCE) was served as the reference electrode, a Pt plate as an auxiliary electrode, and the modified glass carbon electrode (GCE, d = 3 mm) as working electrode. EIS tests were performed in 0.1 M KCl solution containing 5 mM $K_3[Fe(CN)_6]/K_4[Fe(CN)_6]$ (1:1), with an amplitude of 5 mV in a frequency range of 0.01 Hz~100 kHz. CV was conducted in 0.1 M KCl solution containing 5 mM $[Fe(CN)_6]^{3-/4-}$, with scan rate from 10 mV s^{-1} to 200 mV s^{-1}. All measurements were carried out at a steady temperature (25 ± 1 °C).

The AChE-Chit/MXene/Au NPs/MnO_2/Mn_3O_4/GCE biosensor was employed for detecting methamidophos using DPV methods (pulse width, 0.005 s; amplitude, 0.05 V; pulse period, 0.02 s; from 0.1 to 0.9 V). Methamidophos, is a representative organophosphate pesticide. DPV measurements were conducted in PBS (0.1 M, pH 7.4) containing 4 mM ATCl to record the response of the AChE biosensor without or with incubation in different concentrations of pesticides. The inhibition efficiency of pesticides was calculated by the relative reduction of electrochemical response:

$$Inhibition\,(\%) = [(I0 - Ii)/I0] \times 100$$

Here, I_0 and I_i refer to the peak current before and after methamidophos inhibition, respectively.

3. Results and discussion

The fabrication process of the AChE-Chit/MXene/Au NPs/MnO_2/Mn_3O_4/GCE biosensor for monitoring methamidophos is illustrated in Scheme 1. In summary, the MXene/Au NPs and MnO_2/Mn_3O_4 were successively deposited onto a glassy carbon electrode (GCE), and then AChE-Chit mixture was immobilized. In order to explore morphology of biosensing interfaces in each step, SEM images of GCE, MnO_2/Mn_3O_4/GCE, MXene/Au NPs/MnO_2/Mn_3O_4/GCE and AChE-Chit/MXene/Au NPs/MnO_2/Mn_3O_4/GCE were provided in Fig. S1 (in Supplementary Materials).

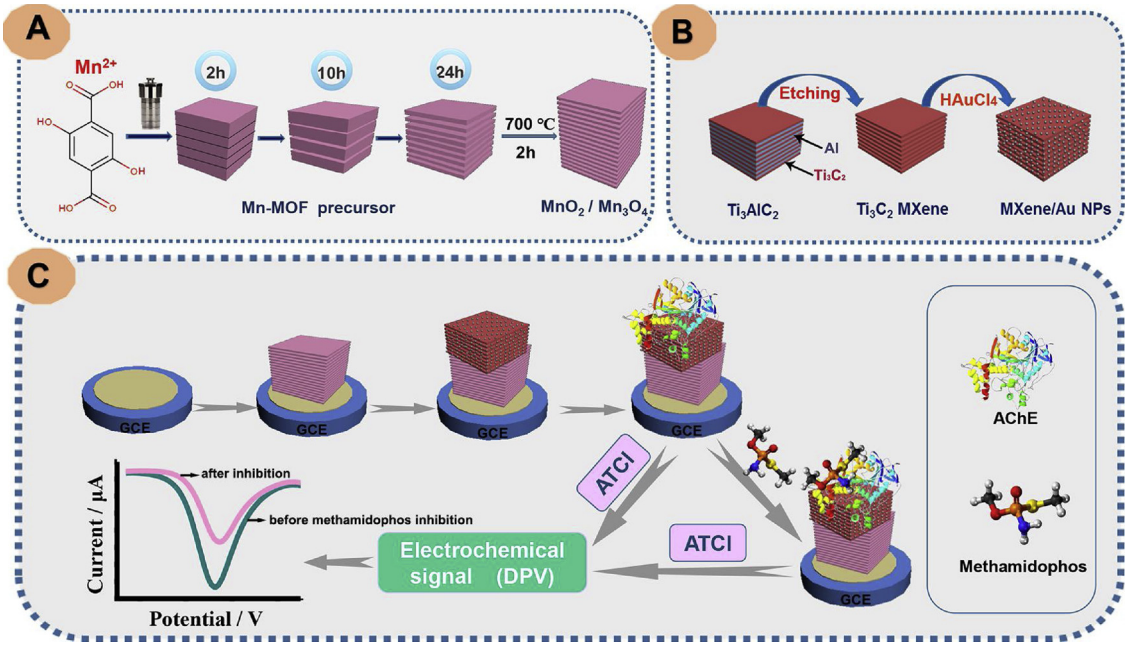

Scheme 1. Illustration of the formation of MnO_2/Mn_3O_4 composite (A), MXene/Au NPs (B), the fabrication process of AChE-Chit/MXene/Au NPs/MnO_2/Mn_3O_4/GCE biosensor for methamidophos assay (C).

3.1. Characterization of MOF-derived MnO_2/Mn_3O_4 composite

The formation of multilayered MnO_2/Mn_3O_4 composite is illustrated in Scheme 1 A. The precursor Mn-MOF composed of orderly stacked layers was prepared by solvothermal reaction without any surfactants added. The growth process of Mn-MOF has been explored with different solvothermal time (Fig. S2 A–C). From the viewpoint of thermodynamics, individual layers which possess high surface energy tend to aggregate vertically to planes to reduce the high surface energy. As a result, the sheets aggregate to generate a layered structure of stacked nanosheets to minimize the overall surface energy. The MOF-derived MnO_2/Mn_3O_4 composite was obtained after Mn-MOF was heat-treated at 700 °C in N_2 gas, in which carbon frameworks partly lost. The morphology and microstructure of the MnO_2/Mn_3O_4 composites were characterized by SEM and TEM. A panoramic view of MnO_2/Mn_3O_4 shown in Fig. S2D indicates that it consists of monodisperse microblocks with sizes of several micrometers. A close observation shows that these microblocks possess an opened interspace and are composed of vertically aligned, highly ordered nanosheets with an average thickness of ~150 nm (Fig. 1A-D). Such well-defined multilayer architecture of MnO_2/Mn_3O_4 composite could provide a large specific surface area. In addition, a high-resolution TEM image (Fig. 1E) clearly illustrates the lattice fringe of 0.495 nm associated with the (101) plane spacing of Mn_3O_4 and 0.238 nm related to the (211) plane spacing of MnO_2, which is in accordance with the following XRD results. As shown in Fig. 1F, the elemental distribution maps of MnO_2/Mn_3O_4 composites clearly demonstrate the homogeneous distribution of Mn (blue) and O (green).

Thermogravimetric analysis (TGA) was employed to study the thermal behavior of Mn-MOF. As what can be seen in Fig. S3, the mass loss is ascribed to the oxidation of the ligands as well as the decomposition of skeleton. Consequently, 700 °C was selected as the calcination temperature to ensure the transformation of Mn-MOF precursors to metal oxides products. The composition and structure of as-prepared Mn-MOF and their derived MnO_2/Mn_3O_4 are confirmed by X-ray powder diffraction (XRD) measurement. The XRD pattern of Mn-MOF (Fig. S4) is in accordance with previous reports [46]. The XRD results of MOF-derived manganese oxide are shown in Fig. 2A. The main diffraction peaks of MnO_2/Mn_3O_4 composite can be indexed to the (110), (200), (310), (400), (211), (411), (521) lattice planes of MnO_2 (JCPDS No. 44-0141) and (101), (112), (200), (103), (211), (220), (224) lattice planes of Mn_3O_4 (JCPDS No. 18-0803), implying that the derivative is a mixed-phase material composed of MnO_2 and Mn_3O_4 phases. To further investigate the electronic state and chemical composition, X-ray photoelectron spectrum (XPS) was carried out. In the full-survey-scan spectrum in Fig. S5 A, the characteristic peaks of Mn, C, and O were observed, confirming the presence of these three elements in the composite. The oxidation state of Mn in manganese oxides was confirmed by the separation energy between Mn 3 s doublet peaks, and it was obtained as 5.01 eV (Fig. S5B), manifesting an intermediate oxidation state between Mn^{3+} and Mn^{4+} [47]. As shown in Fig. 2B, the high-resolution XPS spectrum of Mn 2p is deconvoluted into four peaks at 640.6 eV, 642.1 eV, 652.8 eV and 654.9 eV A couple of peaks at 642.1 eV and 654.9 eV arises from Mn^{III} cations, suggesting the existence of Mn_3O_4 in the composite [48]. Fig. 2C presents the O 1 s spectrum, which is deconvoluted into four peaks with binding energies at 529.8 eV, 531.0 eV, 532.4 eV and 533.5 eV. The peak at 529.8 eV is generally relevant to metal-oxygen bonds (Mn − O), while 531.0 eV possibly correspond to defects, undercoordinated lattice oxygen, or chemisorbed oxygen surface species. Additionally, the peak at 532.4 eV is related to physi/chemisorbed water and another peak at 533.5 eV is ascribed to C − O bonds. The composite was further investigated by Raman spectroscopy. From Fig. S6, the Raman spectrum presents a D band located at 1327 cm^{-1} (sp^3 defects emanating from disordered carbon) as well as a G band situated at 1581 cm^{-1} (sp^2-hybridized graphitic carbon). The intensity of G peak and D peak has similar values with an IG/ID band intensity ratio of ~ 0.983, which implies the graphitization degree of the carbon for the composite.

3.2. Characterization of Ti_3C_2 MXene and MXene/Au NPs

The formation of MXene/Au NPs composite is illustrated in Scheme 1B. Firstly, Ti_3C_2 MXene was prepared by selective etching of the Al layer from Ti_3AlC_2 powders, generating an opened interspace. As shown in the SEM image in Fig. 3(A,B), the synthesized Ti_3C_2 MXene

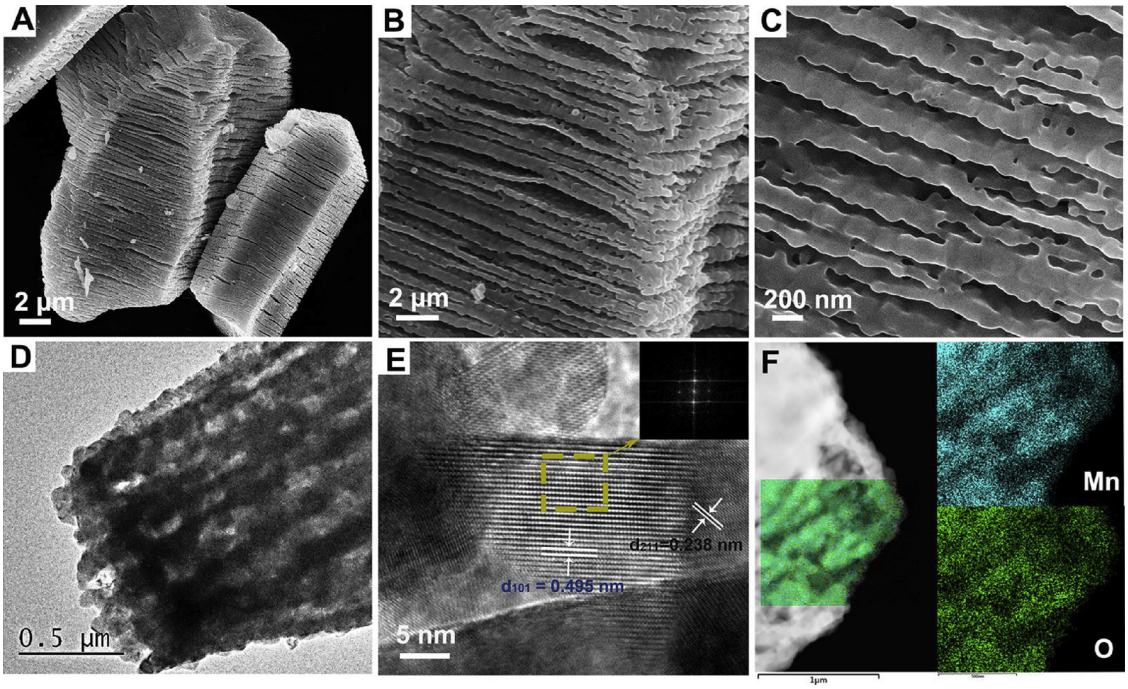

Fig. 1. Morphology and structure characterization. (A–C) SEM images with different magnifications of MnO_2/Mn_3O_4. (D) TEM image of MnO_2/Mn_3O_4. (E) High-resolution TEM image of MnO_2/Mn_3O_4, the corresponding FFT pattern is shown in the inset. (F) HAADF-STEM image of MnO_2/Mn_3O_4 with elemental mapping analyses of Mn (blue), O (green) (For interpretation of the references to colour in this figure legend, the reader is referred to the web version of this article).

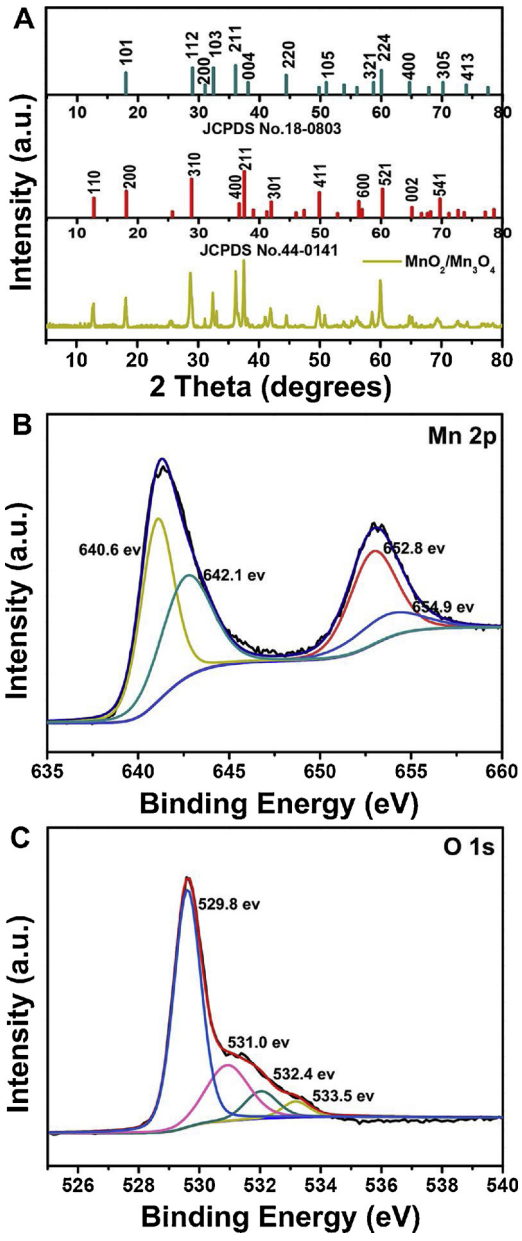

Fig. 2. (A) XRD patterns of MnO_2/Mn_3O_4. (B) and (C) XPS spectra of Mn2p and O1 s.

shows an accordion-like structure along with the exfoliated multilayers less than 50 nm. Interestingly, the unique 2D multilayer nanostructure of Ti_3C_2 MXene could provide a large specific surface area. As shown in Fig. 3(C–E), Au nanoparticles were homogenously absorbed on the surface of MXene with an average size of 10 nm. The XRD patterns of MXene and MXene/Au NPs are shown in Fig. 3F. There are four major characteristic peaks in XRD pattern of MXene/Au NPs, which could be assigned to the (111), (200), (220), and (331) lattice planes of the face-centered-cubic Au single crystal.

3.3. Electrochemical behavior of modified electrodes

Electrical conductivity, electroactive surface area (A), and electrochemical activity, are dominating critical factors of nanomaterials, which greatly impact their performance as electrode material for electrochemical sensors. Hence, CV and EIS measurements were utilized for characterizing these interfacial electrochemical properties of bare GCE, MXene/Au NPs, MnO_2/Mn_3O_4, MXene/Au NPs/MnO_2/Mn_3O_4 modified electrodes, using $[Fe(CN)_6]^{3-/4-}$ as redox probe. Fig. 4A shows the typical Nyquist plots of different modified electrodes, which include a semicircle section at higher frequencies representing electron-transfer-limited process and a linear portion at lower frequency corresponding to the diffusion-limited process. The electron-transfer resistance (Ret), pointing to the electron-transfer kinetics of the $[Fe(CN)_6]^{3-/4-}$ redox probe on the electrodes surface, could be measured by the semicircle diameter. Evidently, both MnO_2/Mn_3O_4 and MXene/Au NPs-modified electrodes possessed a much smaller Ret (108 Ω, 48 Ω) in comparison with that bare GC electrode (410 Ω), indicating improved charge transfer kinetics with the addition of these two composites (Fig. 4A). Besides, the MOF-derived MnO_2/Mn_3O_4/GCE shows a much smaller Ret than Mn-MOF/GCE (Fig. S7), suggesting the improved conductivity of the transition metal oxide compared to the parent Mn-MOF. Incorporation of both MXene/Au NPs and MnO_2/Mn_3O_4, it displays a significantly smaller semicircle and Ret (12 Ω), ascribed to the synergistic effect and excellent conductivity. The results reveal that the combination of MXene/Au NPs and MnO_2/Mn_3O_4 acts as transducer could accelerate electron transfer in electrochemical reactions. After the immobilization of AChE, the Ret value obviously increased, implying that AChE has been successfully immobilized onto the modified electrode. The Ret values of bare and modified electrodes were shown in Fig. 4C.

All CV curves show a pair of well-defined reversible redox peaks in Fig. 4B, which is relevant to Fe^{3+}/Fe^{2+} redox probe. Compared to bare GCE (curve a), a significant increase of reversible redox peak currents and a decrease of peak potential separation (ΔEp) were observed after immobilization of MnO_2/Mn_3O_4 (curve b) or MXene/Au NPs composites (curve c). When simultaneously incorporated with MXene/Au NPs and MnO_2/Mn_3O_4 onto GCE, the reversible redox peak currents significantly increased and ΔEp decreased to minimum value of 0.103 V (curve d). Thus, improved reversibility of redox system and high electron transfer rate are acquired for these two composites, which is consistent with the EIS results. This phenomenon is possibly on account of the synergistic effect of distinguished electrical conductivity and large surface area of MXene/Au NPs and MnO_2/Mn_3O_4. However, when AChE is assembled on the modified electrode (curve e), the peak currents dramatically decreased and ΔEp increased, owing to AChE could severely block the electron transfer of $[Fe(CN)_6]^{3-/4-}$.

Electrochemically active surface area (A) was further measured by CV with different scan rates in 0.1 M KCl solution containing 5 mM $[Fe(CN)_6]^{3-/4-}$. As what can be seen in Fig. 4D-F, both anodic and cathodic peak currents increased with the increase of scan rate, demonstrating the process is controlled by diffusion. Meanwhile, the peak potential obviously shifted and the peak-to-peak potential separation gradually increased. Furthermore, anodic as well as cathodic peak currents increased proportionally to the square root of scan rate ($\upsilon^{1/2}$), respectively. The active surface area of different modified electrodes was calculated by Randles–Sevcik equation [49],

$$i_p = (2.69 \times 10^5) n^{3/2} A D^{1/2} c \upsilon^{1/2}$$

Where n is the number of electrons taking part in the reaction of the $[Fe(CN)_6]^{3-/4-}$ system (n = 1), A represents the area of electrode, D is the diffusion coefficient (6.7×10^{-6} $cm^2 s^{-1}$) and c is the concentration of $[Fe(CN)_6]^{3-/4-}$ (c = 5.0 mM). From the slope of $i_p \sim \upsilon^{1/2}$, the active surface area of MnO_2/Mn_3O_4/GCE, MXene/Au NPs/GCE and MXene/Au NPs/MnO_2/Mn_3O_4/GCE, were obtained as 0.285, 0.394, 0.583 cm^2, respectively. The calculated results indicate that the combination of MXene/Au NPs and MnO_2/Mn_3O_4 can be a good alternative which could provide extremely large active surface area for electrochemical reaction.

3.4. Optimization studies of the biosensor

For the sake of improving the performance of biosensor, several

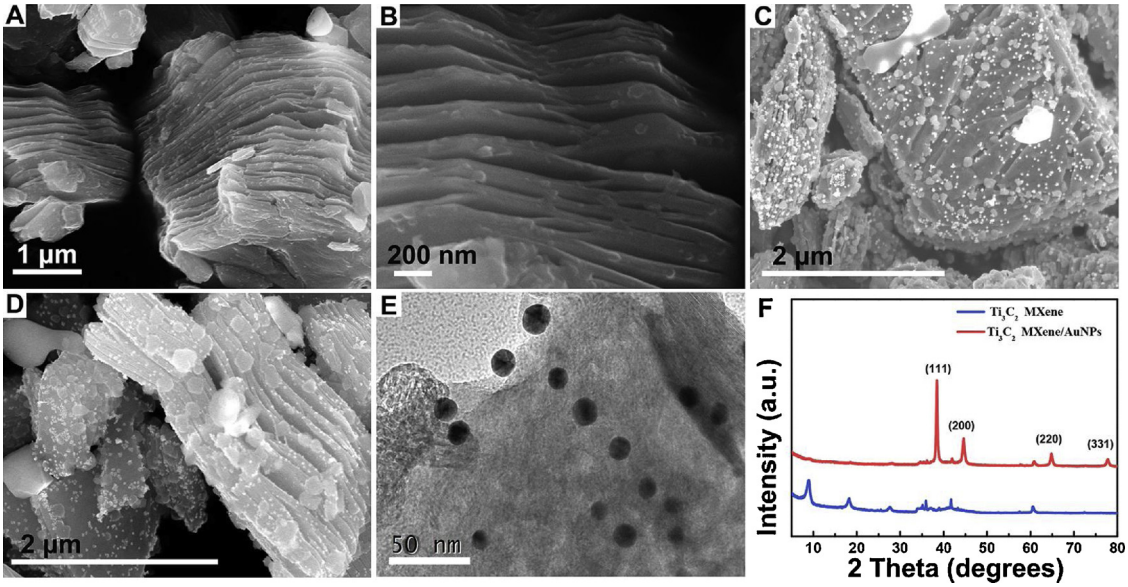

Fig. 3. Morphology and structure characterization. (A,B) SEM images with different magnifications of Ti_3C_2 MXene nanosheets, (C,D) SEM images with different magnifications of Ti_3C_2 MXene/Au NPs. (E) TEM image of Ti_3C_2 MXene/Au NPs. (F) XRD patterns of Ti_3C_2 MXene and Ti_3C_2 MXene/Au NPs.

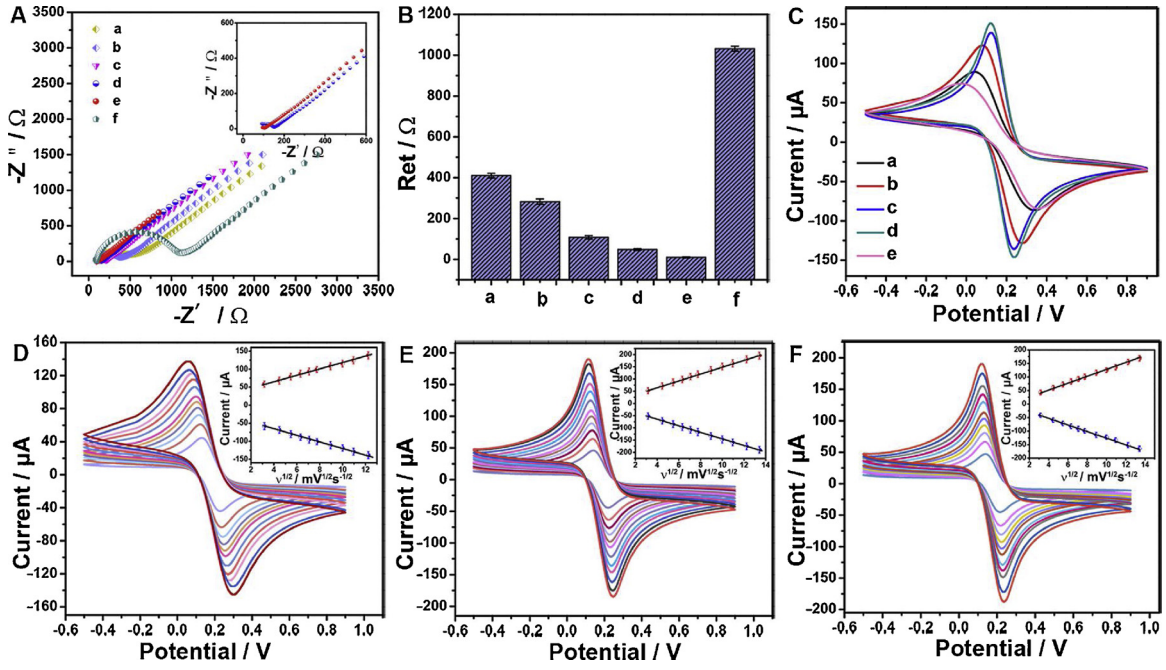

Fig. 4. (A) Nyquist plots of GCE (a), MnO_2/Mn_3O_4/GCE (b), MXene/Au NPs/GCE (c), MXene/Au NPs/MnO_2/Mn_3O_4/GCE (d) and AChE-Chit/MXene/Au NPs/MnO_2/Mn_3O_4/GCE (e), in 0.1 M KCl solution containing 5 mM $[Fe(CN)_6]^{3-/4-}$. (B) The histogram for charge transfer resistance (R_{et}) of bare and modified electrodes. (C) Cyclic voltammetry curves of bare and modified electrodes in 0.1 M KCl containing 5 mM $[Fe(CN)_6]^{3-/4-}$ at scan rate of 100 mV s^{-1}. (D), (E) and (F), Cyclic voltammetry curves of MnO_2/Mn_3O_4/GCE, MXene/Au NPs/GCE and MXene/Au NPs/MnO_2/Mn_3O_4/GCE in 0.1 M KCl containing 5 mM $[Fe(CN)_6]^{3-/4-}$ at different scan rates. Inset (D), (E) and (F) Plots of peak current vs square root of scan rate ($\nu^{1/2}$). Error bars are coefficient of variation across three repetitive experiments (n = 3). Error bars are graphical representations of the variability of data and used on graphs to indicate the error or uncertainty in a reported measurement.

experimental parameters were optimized. The performance of an enzyme-based biosensor is largely dependent on the amount of AChE, which is used as the bio-recognition element. Hence, to choose an optimal amount of AChE for constructing the biosensor was set for the first phase of this work. Biosensors were fabricated with different loading amounts of AChE from 0.05 U to 0.25 U and amperometric responses were recorded in 0.1 M pH 7.4 PBS solution containing 3.5 mM ATCl. As what can be seen in Fig. 5A, as the AChE amount increased, the peak current increased gradually. The biggest response current was obtained at 0.2 U. A small quantity of AChE possibly caused insufficiency of enzyme catalysis reaction while excess enzyme might lead to the decrease of the sensitivity of biosensor. Hence, 0.2 U was chosen as the optimal amount of AChE.

Apart from the amount of AChE, the concentration of MXene/Au NPs and MnO_2/Mn_3O_4 exerts a powerful influence over the sensing performance. The MXene/Au NPs and MnO_2/Mn_3O_4 composite act as transducers for facilitating electron transfer, which could further improve the sensitivity of biosensor and amplify response signal. Hence, it is necessary to ensure optimal loading of the composites onto the electrode surface. Five different concentrations of MXene/Au NPs (0.1,

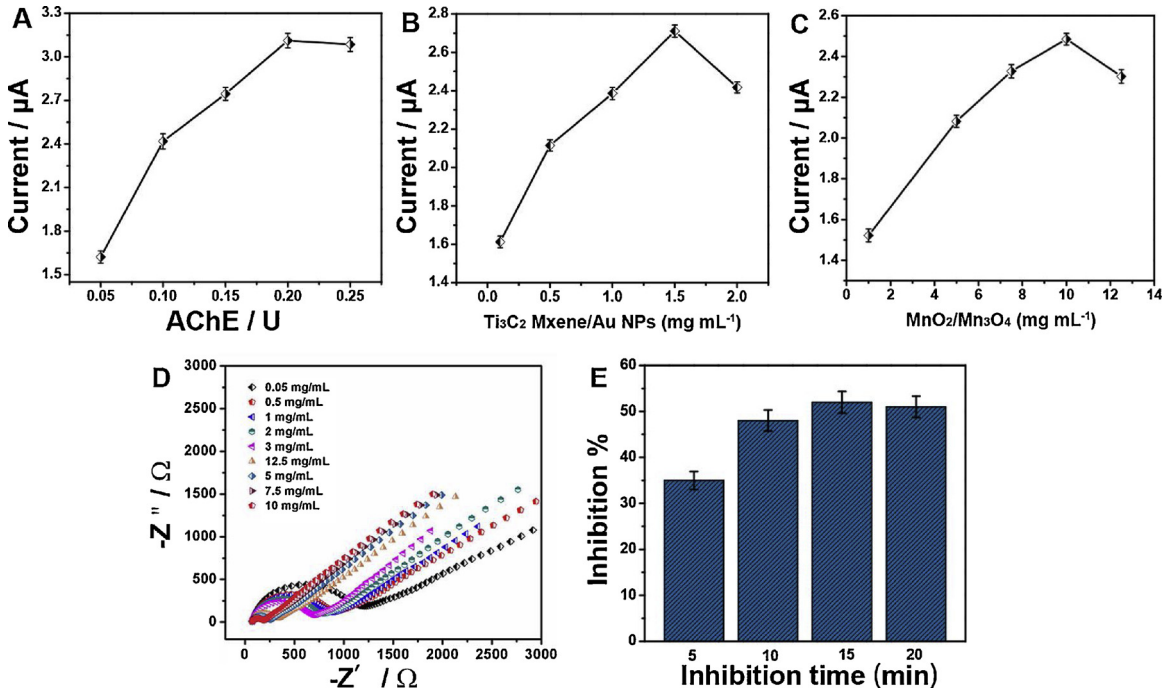

Fig. 5. Effect of (A) AChE amounts, (B) the concentration of Ti_3C_2 MXene/Au NPs, (C) the concentration of MnO_2/Mn_3O_4, (D) Nyquist plots of MnO_2/Mn_3O_4/GCE with different concentrations of MnO_2/Mn_3O_4 composite, (E) inhibition time. Error bars are coefficient of variation across three repetitive experiments (n = 3).

0.5, 1, 1.5, 2 mg mL^{-1}) were examined. Fig. 5B shows that the response current increased monotonically as the concentration increased from 0.1 to 1.5 mg mL^{-1} and then declined over 1.5 mg mL^{-1}. Thus, 1.5 mg mL^{-1} was selected as the optimal concentration of MXene/Au NPs. Likewise, five different concentrations of MnO_2/Mn_3O_4 composite (1, 5, 7.5, 10, 12.5 mg mL^{-1}) were explored. As shown in Fig. 5C, the optimum concentration of MnO_2/Mn_3O_4 composite to be deposited is 10 mg mL^{-1}. High concentration may generate excess materials deposited, as a result of creating a barrier and blocking electron transfer.

In addition, EIS measurements were further utilized to verify the interfacial electrochemical properties of different concentrations of MnO_2/Mn_3O_4 composite modified electrodes. Nine different

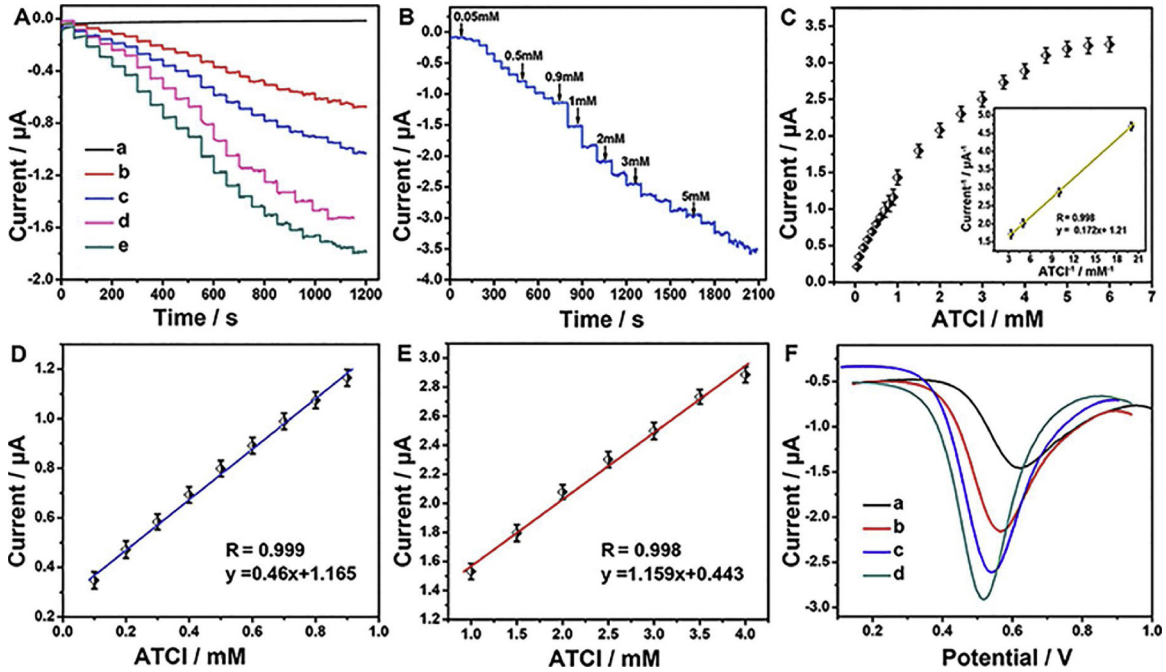

Fig. 6. (A) Amperometric responses of AChE-Chit/GCE (b), AChE-Chit/MnO_2/Mn_3O_4/GCE (c), AChE-Chit/MXene/Au NPs/GCE (d), AChE-Chit/MXene/Au NPs/MnO_2/Mn_3O_4/GCE (e) by successive addition of ATCl in 0.1 M pH 7.4 PBS with a mild stirring; applied potential: 0.55 V vs Ag/AgCl, (a) without adding ATCl. (B) Amperometric responses of AChE-Chit/MXene/Au NPs/MnO_2/Mn_3O_4/GCE by successive addition of ATCl with varying concentrations. (C) Relationship between the obtained reduction peak current and ATCl concentration. Inset C shows the Lineweaver-Burk plot of 1/Iss vs. 1/C. (D) and (E) show the calibration curves for ATCl determination. (F) DPV responses of AChE-Chit/GCE (a), AChE-Chit/MnO_2/Mn_3O_4/GCE (b), AChE-Chit/MXene/Au NPs/GCE (c), AChE-Chit/MXene/Au NPs/MnO_2/Mn_3O_4/GCE (d) in 0.1 M pH 7.4 PBS solution containing 2.5 mM ATCl. Error bars are coefficient of variation across three repetitive experiments (n = 3).

concentrations (0.05, 0.5, 1, 2, 3, 5 7.5, 10, 12.5 mg mL^{-1}) were examined. From Fig. 5D, with the increase of MnO_2/Mn_3O_4 from 0.05 to 10 mg mL^{-1}, the semicircle diameter decrease continuously, indicating the improved electrical conductivity and faster electron transfer. Nevertheless, the semicircle diameter increases over 10 mg mL^{-1}, which might imply saturation of the electrode surface. The results further demonstrate that excess loading amount of MnO_2/Mn_3O_4 composite exerts a barrier and hinders electron transfer.

Furthermore, the responses of the proposed biosensor was investigated with respect to the inhibition time. Organophosphate pesticides could irreversibly inhibit AChE by binding with the active site of the AChE. Hence, sufficient time for pesticides to inhibit the activity of AChE is very essential. Four different inhibition times (5, 10, 15, 20 min) were selected. As shown in Fig. 5E, I% at inhibition times of 5 and 10 min exhibited smaller values than 15 min, while 15 and 20 min have an similar I% results, with small error bar. In consideration of efficiency, 15 min was chosen as the optimum inhibition time.

3.5. Amperometric detection of ATCl

To evaluate the electrochemical responses of the AChE-based biosensors towards ATCl, different materials including MXene/Au NPs and MnO_2/Mn_3O_4 were applied for the construction of biosensor. Fig. 6A shows the amperometric responses of different biosensors with successive addition of ATCl. Both the MXene/Au NPs and MnO_2/Mn_3O_4 composites enhanced the electrochemical responses of the enzymatic biosensors as compared to the AChE-Chit/GCE biosensor without materials. More intriguingly, higher response currents were observed on the MXene/Au NPs/MnO_2/Mn_3O_4-based biosensor than the biosensors based on only one material, which could be account for synergistic signal amplification effect between different components. The amperometric responses of AChE-Chit/MXene/Au NPs/MnO_2/Mn_3O_4/GCE by successive addition of ATCl with varying concentrations were shown in Fig. 6B and the relationship between oxidation current and ATCl concentration was shown in Fig. 6C. It can be observed that with the increasing ATCl concentration, the oxidation current gradually increases.

As what can be seen in Fig. 6D,E a good liner relationship was obtained between the oxidation current (I) and ATCl concentration (C), in wide ranges of 0.05 ~ 1 mM and 1 ~ 4 mM. The calibration equations are I (μA) = 0.46C (mM) + 1.165 (R = 0.999, n = 3) and I (μA) = 1.159C (mM) + 0.443 (R = 0.998, n = 3), respectively. The Michaelis − Menten constant (K_m) was used to describe the enzyme − substrate kinetics and calculated by the Lineweaver–Burk equation [50]. K_m and affinity are inversely related, that is, a smaller K_m implies the immobilized enzyme with a higher affinity towards ATCl. The K_m value for AChE-Chit/MXene/Au NPs/MnO_2/Mn_3O_4/GCE biosensor was obtained as 142 μM, which is obviously smaller than 257.67 μM [51], 0.27 mM [50], 1.39 mM [52], 3.1 mM [21] reported previously, and it demonstrated a higher affinity towards ATCl. Electrochemical performance of different materials modified biosensor toward ATCl was further examined by DPV. Fig. 6F shows the DPV results agree with the amperometric responses towards ATCl. Apparently, the MXene/Au NPs/MnO_2/Mn_3O_4-modified electrode shows the lowest working potential as well as the biggest current. The excellent performance likely results from the synergistic effects between the two components.

3.6. Determination of methamidophos

DPV responses of the AChE-Chit/MXene/Au NPs/MnO_2/Mn_3O_4/GCE biosensor before (a) and after inhibition (b–g) with different concentrations of methamidophos are shown in Fig. 7A. With increasing exposure to methamidophos, the peak current generated from electrochemical oxidation of thiocholine decreased, for the reason that methamidophos could irreversibly inhibit the activity of AChE. Methamidophos could covalently bond with the hydroxyl of the serine in the active site, and then AChE gets phosphorylated, leading to a decrease of AChE activity. Fig. 7B presents the corresponding calibration curve, demonstrating that the inhibition rate (I) is linearly relied on the logarithm of the methamidophos concentration (log C) ranging from 10^{-12} M to 10^{-6} M. The linear regression equation is y = -5.89x + 85.82, with a correlation coefficient R = 0.995. The limit of detection (LOD) of the proposed biosensor for methamidophos determination was 1.34×10^{-13} M. Moreover, this value is much lower than the maximum residue limits (MRLs) permitted by European Union (0.01 mg/kg). Relevant biosensors constructed for detecting methamidophos with respect to the limit of detection, linear range, detection method and immobilization method of AChE were summarized in Table 1. Obviously, the proposed biosensor exhibited remarkable sensing performance in comparison with previous literature.

To investigate that the proposed MXene/Au NPs/MnO_2/Mn_3O_4-based sensing system can be employed not only for monitoring methamidophos but also for other OPs, three other common pesticide (malathion, parathion-methyl and chlorpyrifos) were also tested. As shown in Fig. S8, the inhibition percent of different pesticide with the same concentration of 10^{-6} M were recorded as 52.4%, 41.1%, 43.7% and 47.4% for methamidophos, malathion, parathion-methyl and chlorpyrifos, demonstrating that the proposed biosensor generally applies to OPs.

In chemical analysis, matrix usually refers to some components in a sample, other than the target analyte. The matrix could have a considerable effect on the results of the detection of analytes, that is, qualitative and quantitative errors generated from these components [56–59]. Therefore, matrix effect should be considered. The matrix effect of methamidophos in the orange matrix was calculated as 15% and it showed a weak matrix enhancement effect (in Supplementary material).

To further verify the practical applicability of the as-prepared biosensor, it was employed for methamidophos detection in real samples. The fresh fruit was purchased from a local supermarket and treated by a Chinese Official Standard Method (in Supplementary material). Recovery results were listed in Table S1. Recovery percentages were

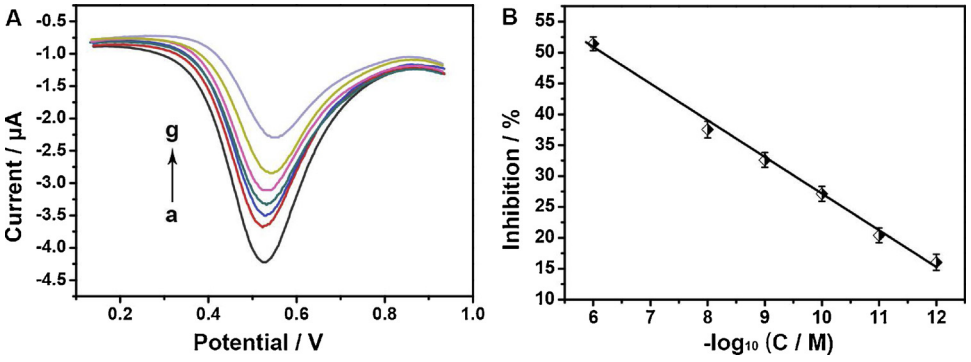

Fig. 7. (A) DPV currents of the AChE-Chit/MXene/Au NPs/MnO_2/Mn_3O_4/GCE after inhibition with different concentrations of methamidophos (a − g): 0, 10^{-6}, 10^{-8}, 10^{-9}, 10^{-10}, 10^{-11}, and 10^{-12} M. (B) Calibration curves for methamidophos determination. Error bars are coefficient of variation across three repetitive experiments (n = 3).

Table 1
Comparisons of the as-prepared biosensors with other biosensors for the determination of methamidophos.

Biosensors	Linear range	Detection limit	Detection method	Immobilization method of AChE	References
AChE/TCNQ/SPE	3.54 nM–0.7 μM	7.08×10^{-9} M	Amperometric	Entrapment	[53]
AChE/Au NPs/Chi/GCE	28×10^{-3}–170×10^{-3} μM	7×10^{-9} M	CV	Covalent	[54]
AChE/Pt–CAs/BDD	10^{-11}–10^{-6} M	3.1×10^{-13} M	DPV	Electrostatic interaction	[55]
AChE-Chit/MXene/Au NPs/MnO_2/Mn_3O_4/GCE	10^{-12}–10^{-6} M	1.34×10^{-13} M	DPV	Covalent	This work

obtained as 95.2%–101.3%, and relative standard deviations (RSDs) were all below 5%, which manifest that the fabricated biosensor is feasible and responsive for monitoring methamidophos in real samples.

3.7. Repeatability, reproducibility, stability and selectivity

The operational repeatability of this biosensor was tested by using the DPV technique of a prepared AChE-Chit/MXene/Au NPs/MnO_2/Mn_3O_4/GCE in pH 7.4 PBS containing 1.0 mM ATCl. RSD of the proposed biosensor was 4.2% for five successive measurements. Similarly, five parallel-prepared MXene/Au NPs/MnO_2/Mn_3O_4-modified electrodes were applied for DPV measurements under the same conditions, with a RSD of 3.6%. The results reveal that this biosensor shows acceptable repeatability and reproducibility. The AChE-based electrode was stored in a refrigerator (4 °C). Amperometric responses of the fabricated biosensor retained approximately 90.4% of its origin value after two weeks of storage, and amperometric responses of AChE-Chit/MXene/Au NPs/MnO_2/Mn_3O_4/GCE in 0.1 M PBS containing 1.0 mM ATCl has been recorded for 20,000 s (Fig. S9). However, amperometric responses of the fabricated biosensor retained 80.7% of its origin value after three weeks of storage. Hence, the test lifetime of the proposed biosensor was evaluated as about two weeks. The results indicate that the biosensor possess a favorable environmental and chemical stability for the further practical application. Experiments were performed to evaluate selectivity of the biosensor by directly injecting some common biological species and electrolytes in the electrochemical cell and recording the amperometric responses to ATCl. As shown in Fig. S10, glucose, citric acid, NO_3^-, SO_4^{2-}, PO_4^{3-}, Cu^{2+}, Fe^{3+}, Zn^{2+}, Pb^{2+} were served as control samples. In the presence of these interferents with high concentration, no significant interference was observed in the detection.

4. Conclusion

In summary, a novel, reliable and sensitive biosensor was successfully developed for the electrochemical detection of OPs based on the MnO_2/Mn_3O_4 and MXene/Au NPs composites, via enzymatic inhibition pathway. In particular, the MnO_2/Mn_3O_4 hierarchical microcuboids consist of vertically aligned, highly ordered nanosheets, have been first synthesized via calcination of Mn-MOF as a precursor. Under optimal conditions, AChE-Chit/MXene/Au NPs/MnO_2/Mn_3O_4/GCE showed outstanding performance for methamidophos detection, a wide linear range from 10^{-12} M to 10^{-6} M with a low detection limit of 1.34×10^{-13} M, which is ascribed to the synergistic effect of MnO_2/Mn_3O_4 and MXene/Au NPs composites, exceptionally large specific surface area for electrochemical reaction, excellent biocompatibility in favour of retaining the AChE activity, and extraordinary conductivity which is of benefit to facilitating the electron transfer as well as improving the sensitivity of response. Besides that, good recovery percentages (95.2%–101.3%) were obtained in real sample analysis. This sensitive sensing platform shows great potentials for the on-site analysis of pesticides exposure or detecting other environmentally pollutants.

Acknowledgments

The authors acknowledge the financial support from the National Natural Science Foundation of China (Grant No. 21875205, 21671168) and the Natural Science Foundation of Hebei (Grant No. B2016203498, 17964403D, GCC2014009)

Appendix A. Supplementary data

Supplementary material related to this article can be found, in the online version, at doi:https://doi.org/10.1016/j.jhazmat.2019.03.083.

References

[1] J.M. Abad, F. Pariente, L. Herna´ndez, H.D. Abrun˜a, E. Lorenzo, Determination of organophosphorus and carbamate pesticides using a piezoelectric biosensor, Anal. Chem. 70 (1988) 2848–2855.
[2] W. Mulchandani, P. Chen, J. Mulchandani, K. Wang, Rogers, Biosensors for direct determination of organophosphate pesticides, Biosens. Bioelectron. 16 (2001) 225–230.
[3] H. Shi, G. Zhao, M. Liu, L. Fan, T. Cao, Aptamer-based colorimetric sensing of acetamiprid in soil samples: sensitivity, selectivity and mechanism, J. Hazard. Mater. 260 (2013) 754–761.
[4] H. Wang, J. Wang, C. Timchalk, Y. Lin, Magnetic electrochemical immunoassays with quantum dot labels for detection of phosphorylated acetylcholinesterase in plasma, Anal. Chem. 80 (2008) 8477–8484.
[5] X. Lu, Y.S. Li, L. Tao, D.D. Song, Y.Z. Wang, Y. Li, F.M. Gao, Amorphous metal boride as a novel platform for acetylcholinesterase biosensor development and detection of organophosphate pesticides, Nanotechnology 30 (2019) 055501.
[6] J. Bao, C.J. Hou, M. Chen, J.J. Li, D.Q. Huo, M. Yang, X.G. Luo, Y. Lei, Plant esterase–chitosan/gold nanoparticles–graphene nanosheet composite-based biosensor for the ultrasensitive detection of organophosphate pesticides, J. Agric. Food Chem. 63 (2015) 10319–10326.
[7] D.D. Song, Y.Z. Wang, X. Lu, Y.K. Gao, Y. Li, F.M. Gao, Ag nanoparticles-decorated nitrogen-fluorine co-doped monolayer MoS_2 nanosheet for highly sensitive electrochemical sensing of organophosphorus pesticides, Sens. Actuators B Chem. 267 (2018) 5–13.
[8] X. Ren, T. Zhang, D. Wu, T. Yan, X.H. Pang, B. Du, W.R. Lou, Q. Wei, Increased electrocatalyzed performance through high content potassium doped graphene matrix and aptamer tri infinite amplification labels strategy: highly sensitive for matrix metalloproteinases-2 detection, Biosens. Bioelectron. 94 (2017) 694–700.
[9] L. Yang, W.J. Zhu, X. Ren, M.S. Khan, Y. Zhang, B. Du, Q. Wei, Macroporous graphene capped Fe_3O_4 for amplified electrochemiluminescence immunosensing of carcinoembryonic antigen detection based on CeO_2@TiO_2, Biosens. Bioelectron. 91 (2017) 842–848.
[10] X. Ren, J.R. Yan, D. Wu, Q. Wei, Y.K. Wan, Nanobody-based apolipoprotein e immunosensor for point-of-care testing, ACS Sens. 2 (2017) 1267–1271.
[11] H.M. Ma, Y.H. Zhao, Y.Y. Liu, Y. Zhang, D. Wu, H. Li, Q. Wei, A compatible sensitivity enhancement strategy for electrochemiluminescence immunosensors based on the biomimetic melanin-like deposition, Anal. Chem. 89 (2017) 13049–13053.
[12] L. Yang, Y.Y. Li, Y. Zhang, D.W. Fan, X.H. Pang, Q. Wei, B. Du, 3D nanostructured palladium-functionalized graphene-aerogel-supported Fe_3O_4 for enhanced Ru $(bpy)_3^{2+}$-based electrochemiluminescent immunosensing of prostate specific antigen, ACS Appl. Mater. Interfaces 9 (2017) 35260–35267.
[13] X. Lu, L. Tao, Y.S. Li, H.M. Huang, F.M. Gao, A highly sensitive electrochemical platform based on the bimetallic Pd@Au nanowires network for organophosphorus pesticides detection, Sens. Actuators B Chem. 284 (2019) 103–109.
[14] P. Weerathunge, R. Ramanathan, R. Shukla, T.K. Sharma, V. Bansal, Aptamer-controlled reversible inhibition of gold nanozyme activity for pesticide sensing, Anal. Chem. 86 (2014) 11937–11941.
[15] S. Samsidar, S.M. Siddiquee, Shaaram, A review of extraction, analytical and advanced methods for determination of pesticides in environment and foodstuffs, Trends Food Sci. Technol. 71 (2018) 188–201.
[16] X. Ren, H.M. Ma, T. Zhang, Y. Zhang, T. Yan, B. Du, Q. Wei, Sulfur-doped graphene-based immunological biosensing platform for multianalysis of cancer biomarkers, ACS Appl. Mater. Interfaces 9 (2017) 37637–37644.
[17] X.H. Pang, C. Cui, M.H. Su, Y.G. Wang, Q. Wei, W.H. Tan, Construction of self-powered cytosensing device based on ZnO nanodisks@g-C_3N_4 quantum dots and application in the detection of CCRF-CEM cells, Nano Energy 46 (2018) 101–109.
[18] D.D. Song, Q. Li, X. Lu, Y.S. Li, Y. Li, F.M. Gao, Ultra-thin bimetallic alloy nanowires with porous architecture/monolayer MoS_2 nanosheet as a highly sensitive platform for the electrochemical assay of hazardous omethoate pollutant, J. Hazard. Mater.

357 (2018) 466–474.
[19] M.Z.M. Nasir, C.C. Mayorga-Martinez, Z. Sofer, M. Pumera, Two-dimensional 1T-phase transition metal dichalcogenides as nanocarriers to enhance and stabilize enzyme activity for electrochemical pesticide detection, ACS Nano 11 (2017) 5774–5784.
[20] J. Kirsch, C. Siltanen, Q. Zhou, A. Revzin, A. Simonian, Biosensor technology: recent advances in threat agent detection and medicine, Chem. Soc. Rev. 42 (2013) 8733–8768.
[21] H.F. Cui, W.W. Wu, M.M. Li, X. Song, Y. Lv, T.T. Zhang, A highly stable acetylcholinesterase biosensor based on chitosan-TiO_2-graphene nanocompsites for detection of organophosphate pesticides, Biosens. Bioelectron. 99 (2018) 223–229.
[22] S. Dang, Q.L. Zhu, Q. Xu, Nanomaterials derived from metal-organic frameworks, Nat. Rev. Mater. 3 (2017) 17075.
[23] H.-C.J. Zhou, S. Kitagawa, Metal-organic frameworks (MOFs), Chem. Soc. Rev. 43 (2014) 5415–5418.
[24] A.C. McKinlay, J.F. Eubank, S. Wuttke, B. Xiao, P.S. Wheatley, P. Bazin, J.-C. Lavalley, M. Daturi, A. Vimont, G.D. Weireld, Nitric oxide adsorption and delivery in flexible MIL-88(Fe) metal－organic frameworks, Chem. Mater. 25 (2013) 1592–1599.
[25] H. Furukawa, K.E. Cordova, M.O.'. Keeffe, O.M. Yaghi, The chemistry and applications of metal-organic frameworks, Science. 341 (2013) 1230444.
[26] L.E. Kreno, K. Leong, O.K. Farha, M. Allendorf, R.P.V. Duyne, J.T. Hupp, Metal–organic framework materials as chemical sensors, Chem. Rev. 112 (2012) 1105–1125.
[27] K. Vikrant, V. Kumar, Y.S. Ok, K.-H. Kim, A. Deep, Metal-organic framework (MOF)-based advanced sensing platforms for the detection of hydrogen sulfide, Trends Analyt. Chem. 105 (2018) 263–281.
[28] H.C. Zhou, J.R. Long, O.M. Yaghi, Introduction to metal–organic frameworks, Chem. Rev. 112 (2012) 673–674.
[29] L. Zhao, B.L. Dong, S.Z. Li, L.J. Zhou, L.F. Lai, Z.Z. Wang, S.L. Zhao, M. Han, K. Gao, M. Lu, X.J. Xie, B. Chen, Z.D. Liu, X.J. Wang, H. Zhang, H. Li, J.Q. Liu, H. Zhang, X. Huang, W. Huang, Interdiffusion reaction-assisted hybridization of two-dimensional metal–organic frameworks and $Ti_3C_2T_x$ nanosheets for electrocatalytic oxygen evolution, ACS Nano 11 (2017) 5800–5807.
[30] Q.L. Zhu, Q. Xu, Metal–organic framework composites, Chem. Soc. Rev. 43 (2014) 5468–5512.
[31] Y.V. Kaneti, J. Tang, R.R. Salunkhe, X. Jiang, A. Yu, K.C.W. Wu, Y. Yamauchi, Nanoarchitectured design of porous materials and nanocomposites from metal-organic frameworks, Adv. Mater. 29 (2017) 1604898–1604938.
[32] R.R. Salunkhe, J. Tang, Y. Kamachi, T. Nakato, J.H. Kim, Y. Yamauchi, Asymmetric supercapacitors using 3D nanoporous carbon and cobalt oxide electrodes synthesized from a single metal–organic framework, ACS Nano 9 (2015) 6288–6296.
[33] J. Zhou, Y.B. Dou, A.W. Zhou, L. Shu, Y. Chen, J.R. Li, Layered metal－organic framework-derived metal oxide/carbon nanosheet arrays for catalyzing the oxygen evolution reaction, ACS Energy Lett. 3 (2018) 1655–1661.
[34] R.R. Salunkhe, Y.V. Kaneti, Y. Yamauchi, Metal–organic framework-derived nanoporous metal oxides toward supercapacitor applications: progress and prospects, ACS Nano 11 (2017) 5293–5308.
[35] B. Anasori, Y. Xie, M. Beidaghi, J. Lu, B.C. Hosler, L. Hultman, P.R.C. Kent, Y. Gogotsi, M.W. Barsoum, Two-dimensional, ordered, double transition metals carbides (MXenes), ACS Nano 9 (10) (2015) 9507–9516.
[36] M. Naguib, V.N. Mochalin, M.W. Barsoum, Y. Gogotsi, Two-dimensional materials: 25th anniversary article: MXenes: a new family of two-dimensional materials, Adv. Mater. 26 (2014) 992–1005.
[37] M.R. Lukatskaya, O. Mashtalir, C.E. Ren, Y. Dall'Agnese, P. Rozier, P.L. Taberna, M. Naguib, P. Simon, M.W. Barsoum, Y. Gogotsi, Cation intercalation and high volumetric capacitance of two-dimensional titanium carbide, Science. 341 (2013) 1502–1505.
[38] S.L. Zhao, Y. Wang, J.C. Dong, C.-T. He, H.J. Yin, P.E. An, K. Zhao, X.F. Zhang, C. Gao, L.J. Zhang, J.W. Lv, J.X. Wang, J.Q. Zhang, A.M. Khattak, N.A. Khan, Z.X. Wei, J. Zhang, S.Q. Liu, H.J. Zhao, Z.Y. Tang, Ultrathin metal–organic framework nanosheets for electrocatalytic oxygen evolution, Nat. Energy. 1 (2016) 16184.
[39] X. Xie, S. Chen, W. Ding, Y. Nie, Z. Wei, An extraordinarily stable catalyst: Pt NPs supported on two-dimensional $Ti_3C_2X_2$ (X = OH, F) nanosheets for oxygen reduction reaction, Chem. Commun. (Camb.) 49 (2013) 10112–10114.
[40] J.M. Luo, X.Y. Tao, J. Zhang, Y. Xia, H. Huang, L.Y. Zhang, Y.P. Gan, C. Liang, W.K. Zhang, Sn^{4+} ion decorated highly conductive Ti_3C_2 Mxene: promising lithium-ion anodes with enhanced volumetric capacity and cyclic performance, ACS Nano 10 (2016) 2491–2499.
[41] Y.C. Cai, J. Shen, G. Ge, Y.Z. Zhang, W.Q. Jin, W. Huang, J.J. Shao, J. Yang, X.C. Dong, Stretchable Ti_3C_2Tx MXene/carbon nanotube composite based strain sensor with ultrahigh sensitivity and tunable sensing range, ACS Nano 12 (2018) 56–62.
[42] L.X. Wu, X.B. Lu, Z.-S. Dhanjai, Y.F. Wu, X.H. Dong, S.H. Wang, J.P. Zheng, Chen, 2D transition metal carbide MXene as a robust biosensing platform for enzyme immobilization and ultrasensitive detection of phenol, Biosens. Bioelectron. 107 (2018) 69–75.
[43] Q. Hu, H. Wang, Q. Wu, X. Ye, A. Zhou, D. Sun, L. Wang, B. Liu, J. He, Two-dimensional Sc_2C: a reversible and high capacity hydrogen storage material predicted by first-principles calculations, Int. J. Hydrogen Energy 39 (2014) 10606–10612.
[44] C.L. Tan, X.H. Cao, X.J. Wu, Q.Y. He, J. Yang, X. Zhang, J. Chen, W. Zhao, S.H. Han, G.H. Nam, M. Sindoro, H. Zhang, Recent advances in ultrathin two-dimensional nanomaterials, Chem. Rev. 117 (2017) 6225–6331.
[45] M. Ghidiu, J. Halim, S. Kota, D. Bish, Y. Gogotsi, M.W. Barsoum, Ion-exchange and cation solvation reactions in Ti_3C_2 MXene, Chem. Mater. 28 (2016) 3507–3514.
[46] L.L. Wu, Z. Wang, Y. Long, J. Li, Y. Liu, Q.S. Wang, X. Wang, S.Y. Song, X.G. Liu, H.J. Zhang, Multishelled $Ni_xCo_{3-x}O_4$ hollow microspheres derived from bimetal-organic frameworks as anode materials for high-performance lithium-ion batteries, Small 13 (2017) 1604270.
[47] E.S. Ilton, J.E. Post, P.J. Heaney, F.T. Ling, S.N. Kerisit, XPS determination of Mn oxidation states in Mn (hydr)oxides, Appl. Surf. Sci. 366 (2016) 475–485.
[48] Y.T. Chu, L.Y. Guo, B.J. Xi, Z.Y. Feng, F.F. Wu, Y. Lin, J.C. Liu, D. Sun, J.K. Feng, Y.T. Qian, S.L. Xiong, Embedding $MnO@Mn_3O_4$ nanoparticles in an N-doped-carbon framework derived from Mn-organic clusters for efficient lithium storage, Adv. Mater. 30 (2018) 1704244.
[49] D.G. Rackus, M.H. Shamsi, A.R. Wheeler, Electrochemistry, biosensors and microfluidics: a convergence of fields, Chem. Soc. Rev. 44 (2015) 5320–5340.
[50] D. Du, M.H. Wang, J. Cai, Y.H. Qin, A.D. Zhang, One-step synthesis of multiwalled carbon nanotubes-gold nanocomposites for fabricating amperometric acetylcholinesterase biosensor, Sens. Actuators B Chem. 143 (2010) 337–341.
[51] Y.J. Jiang, X.N. Zhang, L.J. Pei, S. Yue, L. Ma, L.Y. Zhou, Z.H. Huang, Y. He, J. Gao, Silver nanoparticles modified two-dimensional transition metal carbides as nanocarriers to fabricate acetycholinesterase-based electrochemical biosensor, Chem. Eng. J. 339 (2018) 547–556.
[52] R.R. Dutta, P. Puzari, Amperometric biosensing of organophosphate and organocarbamate pesticides utilizing polypyrrole entrapped acetylcholinesterase electrode, Biosens. Bioelectron. 52 (2014) 166–172.
[53] P.R.B. de Oliveira Marques, G.S. Nunes, T.C. dos Santos, S. Andreescu, J.L. Marty, Comparative investigation between acetylcholinesterase obtained from commercial sources and genetically modified drosophila melanogaster. Application in amperometric biosensors for methamidophos pesticide detection, Biosens. Bioelectron. 20 (2004) 825–832.
[54] Y.R. Li, Z.Y. Gan, Y.F. Li, Q. Liu, J.C. Bao, Z.H. Dai, Immobilization of acetylcholinesterase on one-dimensional gold nanoparticles for detection of organophosphorous insecticides, Sci. China Chem. 53 (2010) 820–825.
[55] Y. Liu, M. Wei, Development of acetylcholinesterase biosensor based on platinume carbon aerogels composite for determination of organophosphorus pesticides, Food Control 36 (2014) 49–54.
[56] G.F. Pang, C.L. Fan, Q.Y. Chang, F. Yang, Y.Z. Cao, Matrix effect for determination of pesticide residues in tea, Anal. Pesticide Tea 4 (2018) 535–595.
[57] L. Xiang, L. Chen, T. Xiao, C.H. Mo, Y.W. Li, Q.Y. Cai, H. Li, D.M. Zhou, M.H. Wong, Determination of trace perfluoroalkyl carboxylic acids in edible crop matrices: matrix effect and method development, J. Agric. Food Chem. 65 (2017) 8763–8772.
[58] T. Yarita, Y. Aoyagi, T. Otake, Evaluation of the impact of matrix effect on quantification of pesticides in foods by gas chromatography–mass spectrometry using isotope-labeled internal standards, J. Chromatogr. A 1396 (2015) 109–116.
[59] M.R. Jadhav, D.P. Oulkar, T.P.A. Shabeer, K. Banerjee, Quantitative screening of agrochemical residues in fruits and vegetables by buffered ethyl acetate extraction and LC-MS/MS analysis, J. Agric. Food Chem. 63 (2015) 4449–4456.